

# Growth and Termination Dynamics of Multiwalled Carbon Nanotubes at Near Ambient Pressure: An in Situ Transmission Electron Microscopy Study

Xing Huang,<sup>\*,†,‡,§</sup> Ramzi Farra,<sup>†</sup> Robert Schlögl,<sup>†,§</sup> and Marc-Georg Willinger<sup>†,‡,§</sup>

<sup>†</sup>Fritz Haber Institute of Max Planck Society, Faradayweg 4-6, 14195 Berlin, Germany

<sup>‡</sup>Scientific Center for Optical and Electron Microscopy, ETH Zurich, Otto-Stern-Weg 3, 8093 Zurich, Switzerland

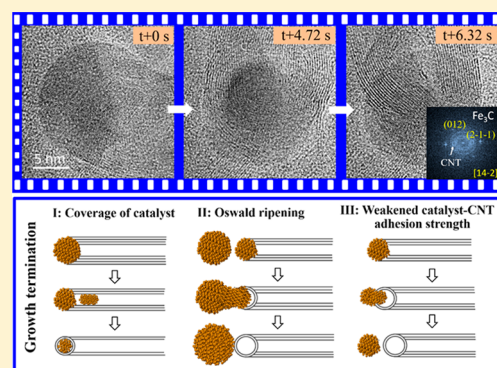
<sup>§</sup>Department of Heterogeneous Reactions, Max Planck Institute for Chemical Energy Conversion, 45470 Mülheim an der Ruhr, Germany

## Supporting Information

**ABSTRACT:** Understanding the growth mechanism of carbon nanotubes (CNTs) has been long pursued since its discovery. With recent integration of in situ techniques into the study of CNT growth, important insights about the growth mechanism of CNT have been generated, which have improved our understanding significantly. However, previous in situ experiments were mainly conducted at low pressures which were far from the practical conditions. Direct information about the growth dynamics under relevant conditions is still absent and thus is highly desirable. In this work, we report atomic-scale observations of multiwalled CNT (MWCNT) growth and termination at near ambient pressure by in situ transmission electron microscopy. On the basis of the real-time imaging, we are able to reveal that the working catalyst is constantly reshaping at its apex during catalyzing CNT growth, whereas at the base the catalyst remains faceted and barely shows any morphological change. The active catalyst is identified as

crystalline Fe<sub>3</sub>C, based on lattice fringes that can be imaged during growth. However, the oscillatory growth behavior of the CNT and the structural dynamics of the apex area strongly indicate that the carbon concentration in the catalyst particle is fluctuating during the course of CNT growth. Extended observations further reveal that the catalyst splitting can occur: whereas the majority of the catalyst stays at the base and continues catalyzing CNT growth, a small portion of it gets trapped inside of the growing nanotube. The catalyst splitting can take place multiple times, leading to shrinkage of both, catalyst size and diameter of CNT, and finally the growth termination of CNT due to the full coverage of the catalyst by carbon layers. Additionally, in situ observations show two more scenarios for the growth termination, that is, out-migration of the catalyst from the growing nanotube induced by (i) Oswald ripening and (ii) weakened adhesion strength between the catalyst and CNT.

**KEYWORDS:** MWCNT, in situ TEM, atomic-scale, catalyst splitting, growth and termination dynamics



Carbon nanotubes (CNTs) have triggered tremendous research interest in the past few decades because of their unique physical and chemical properties as well as their potential uses in electronics, catalysis, energy storage, and so forth.<sup>1,2</sup> Among these well-established approaches<sup>3–5</sup> for synthesis of CNTs, the metal-catalyzed chemical vapor deposition (CVD) has been considered as the most suitable one due to its simplicity, scalability, and higher degree of control.<sup>6,7</sup> In metal-catalyzed CVD process, transition metals such as Ni,<sup>8</sup> Fe,<sup>9,10</sup> and Co<sup>11</sup> are commonly used as catalysts to grow CNTs. For scalable fabrication, binary mixtures of these metals are often employed due to enhanced activity and yield.<sup>12,13</sup> Although industrial-scale production of CNTs has been realized in recent years, we are still suffering from unsatisfactory uniformity and controllability. To obtain desired performances of CNT-based devices, it is essential to synthesize CNTs with controlled diameter, length, and

chirality<sup>14–16</sup> which are key factors in determining the performances. The lack of controllability, to a large extent, is due to limited atomic-scale information on CNT growth and molecular-level understanding of growth mechanism. Some key questions are still waiting for answers or to be clarified,<sup>17</sup> for example, what is the state of the catalyst (liquid or solid), what is the active structure of the catalyst, how external parameters such as temperature or pressure impact growth dynamics of CNTs, and what are the causes for growth termination of CNTs, and so forth.

The recent developments of in situ techniques have enabled unprecedented opportunities for investigating dynamic changes of materials under relevant conditions.<sup>18–21</sup> Using in

**Received:** May 8, 2019

**Revised:** July 15, 2019

**Published:** August 1, 2019

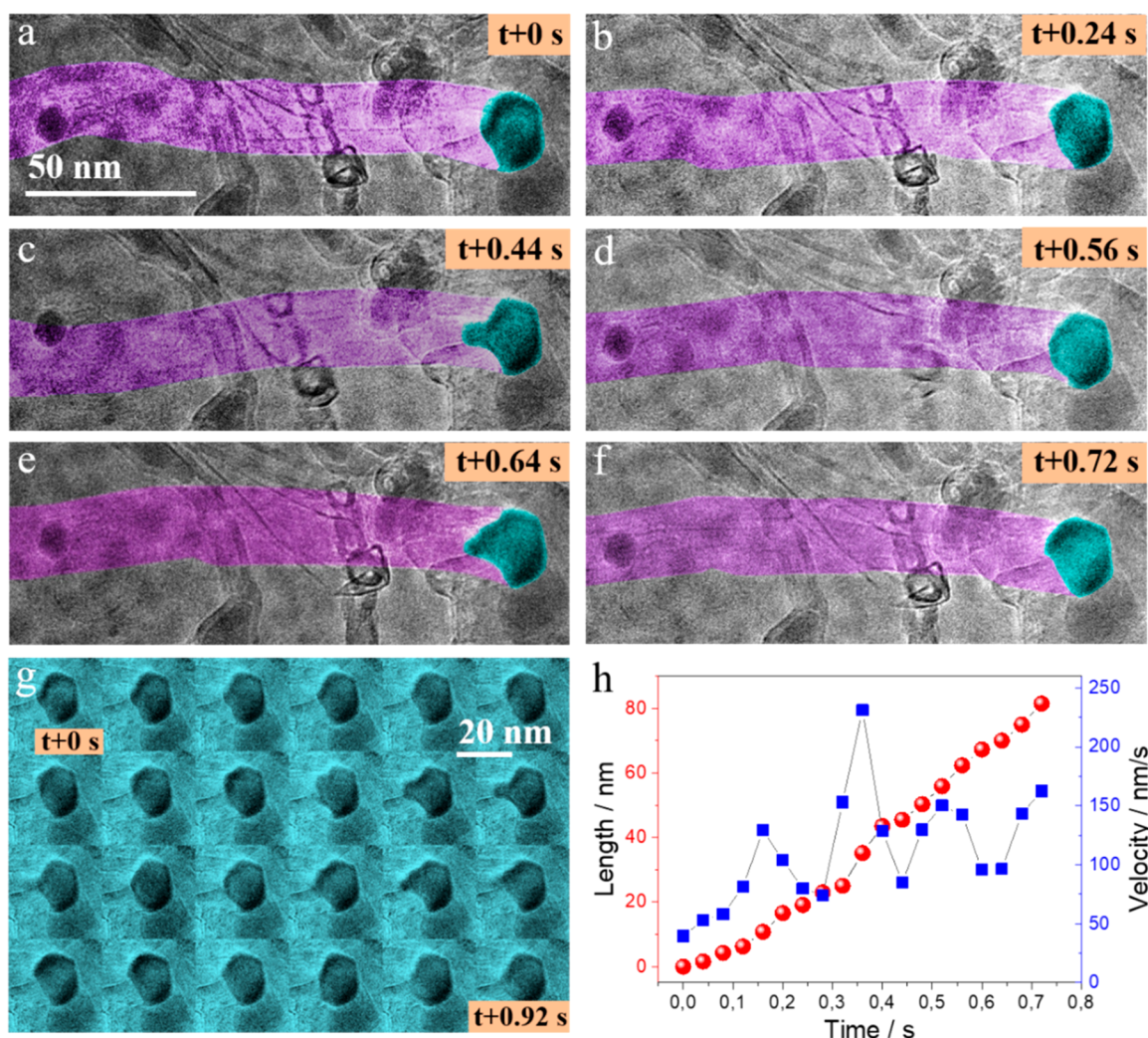


**Figure 1.** (a–f) Sequential TEM images showing dynamic process of a CNT growth from an iron particle. (g) Shape evolution of the catalytic particle during the CNT growth. (h) Length and growth velocity of the CNT as a function of time.

situ X-ray photoelectron spectroscopy, Hoffmann et al. studied the state and structure of the catalyst (Fe, Ni) during CNT growth<sup>22</sup> and claimed that the active catalyst is crystalline metallic nanoparticle. Later on, a combined study<sup>23</sup> based on in situ X-ray diffraction and in situ transmission electron microscopy (TEM) suggested that the active catalyst (in the case of Fe) contains a mixture of Fe and Fe<sub>3</sub>C with the metallic Fe existing in either body-centered cubic (bcc) or face-centered cubic (fcc) structure, depending on its kinetically accessible pathway. In contrast, Yoshida et al. carried out an in situ TEM study of CNT growth using an environmental TEM, from which they exclusively concluded that the catalyst crystallizes as iron carbide during CNT growth.<sup>24</sup> Shortly after, a similar statement was made by Sharma et al.,<sup>25</sup> based on their in situ TEM study. The controversy over the active structure, on one hand, might be related to the different experimental conditions used, such as different carbon precursor, temperature, and pressure, which regulate the structure of the catalyst and the dynamic growth process of CNT with response to the chemical potential of gases. On the other hand, it may originate from the techniques that were employed for investigations. It is known that photon-based spectroscopic techniques provide integrated signals at macro-scale, which may contain information from both active and

inactive states of the catalysts. In contrast, in situ TEM can directly probe the local atomic arrangement of the active catalyst and the associated morphological changes, which ensures the relevance of the obtained information and thus, may lead to a better understanding of CNT growth mechanism.

With most of previous in situ TEM studies conducting at very low pressure ( $10^{-5}$ – $10^{-3}$  bar),<sup>8,24–27</sup> observations of the atomic process of CNT growth at near ambient pressure that is more relevant for industrial synthesis, however, have been rarely reported. Recent development of Micro-Electro-Mechanical System (MEMS) based membrane devices has allowed the performance of in situ TEM experiments at temperatures as high as 1000 °C and pressures up to 1 bar.<sup>28–30</sup> Herein, we implement in situ TEM on visualizing the growth dynamics of MWCNTs from Fe-based catalyst at pressure of 178.65 mbar in a gas mixture of H<sub>2</sub>, C<sub>2</sub>H<sub>4</sub>, and He. On the basis of continuous atomic-scale imaging, we are able to reveal the structure of the active catalyst and its dynamical behaviors during catalyzing CNT growth, which may shed some light on mechanistic understanding of CNT growth. Moreover, in situ observations reveal three different scenarios for the growth termination of CNTs. The present in situ study provides insightful information toward understanding of the

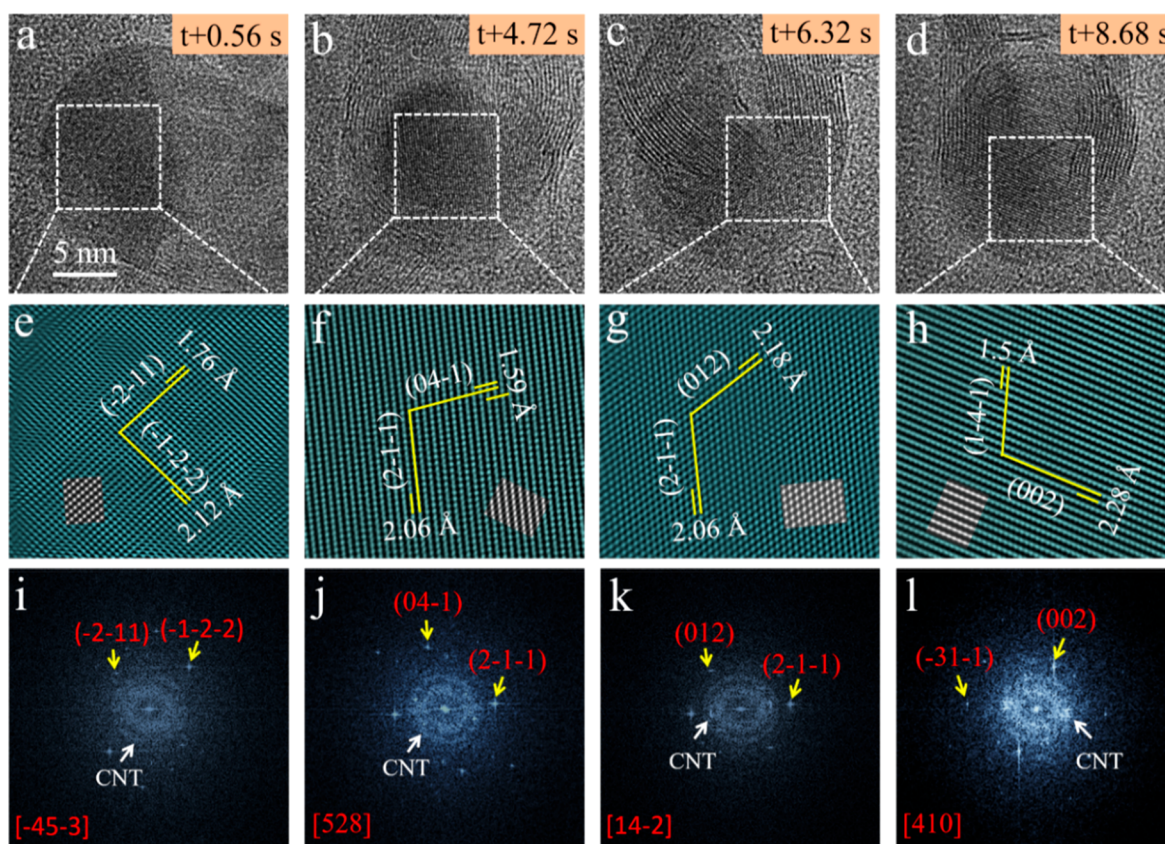


**Figure 2.** Structural analysis of an active catalyst. (a–d) Time-course HRTEM images of an active catalyst recorded while it is catalyzing a CNT growth. (e–h) Fourier-filtered HRTEM images of the catalyst from the rectangle regions marked in (a–d). Lattice fringes of CNT are filtered out. Insets show the simulated HRTEM images. (i–l) FFTs of HRTEM images in (a–d).

growth and termination processes of CNTs, which could serve as an experimental basis for rational design and synthesis of CNTs with improved controllability.

**Results and Discussion.** The in situ experiment is performed inside the column of an aberration-corrected Titan 80-300 TEM (operated at 300 kV) using a MEMS-based in situ gas and heating holder (DENSolutions) and a home-built gas feeding system. The precursor material used for CNT growth is  $\text{Fe}_2\text{O}_3$  (Figure S1), which is first treated in 10%  $\text{H}_2$  at elevated temperatures up to 800 °C. We find the treatment does not lead to reduction of oxide, which may be related to relatively low partial pressure of  $\text{H}_2$  and a large size of oxide particles (up to 1  $\mu\text{m}$ ). In addition, a trace amount of oxygen due to leakage of the setup can presently not be excluded and could thus hinder oxide reduction. Switching from hydrogen to reaction gas (20%  $\text{C}_2\text{H}_4$ , 20%  $\text{H}_2$ , and 60% He) is performed at 150 °C followed by a stepwise increase of the temperature to 800 °C. Because of a higher reduction potential of the reaction gas, the  $\text{Fe}_2\text{O}_3$  is reduced to  $\text{Fe}_3\text{O}_4$  in the temperature regime between 450 and 650 °C. The reduction is accompanied by a collapse of particles into smaller ones (Figure S2). With a further temperature increase, contrast variations due to particle reconstruction or rearrangement are observed until suddenly the onset of CNT growth is observed at around 800 °C (Figure S3). In situ observations of CNT growth and termination were made at 800 °C at a pressure of 178.65 mbar and a flow rate of 0.24 mL/min (details are provided in Experimental Section).

Figure 1a–f shows a few snapshots extracted from Movie 1, which is provided as Supporting Information. One can see how

the multiwalled CNT (MWCNT) evolves from an active and structurally dynamic iron catalyst. Note that the position of the catalyst particle remains almost unchanged, indicating that it is firmly attached to the substrate. This so-called base-growth<sup>31</sup> is generally observed when the interaction between the catalyst and substrate is strong. In this study, the silicon nitride membrane of the MEMS chip or nonreactive larger-sized particles can serve as substrates and keep catalytic particles in place. In situ TEM observation also uncovers that while the base of the catalyst remains faceted and barely shows any morphological change during CNT growth, the apex of the catalyst (where the CNT sprouts out) shows a fast, constant deformation (Figure 1g). Although partially behaving like a liquid, the whole catalytic particle (including the base and the apex of the catalyst) clearly delivers a diffraction contrast during the course of CNT growth, which is a strong indication for the solid state of the catalyst.

To gain some mechanistic insights from the growth kinetics of CNT, we measure the length of CNT as a function of time (Figure 1h). The growth rate can then be further obtained by performing the time-derivative of the measured growth length (details for growth length and velocity determinations are provided in Supporting Information). One can see that the CNT grows about 80 nm in 0.72 s (about 111 nm/s), which is much faster than the growth speed reported for low pressures and temperatures.<sup>24,25</sup> It is further found that the growth velocity of CNT varies in an oscillatory fashion, suggesting a periodical change in desorption rate of carbon at the CNT/catalyst interface. It is worth to mention that we have tried to abstract a relation between the catalyst particle size and CNT

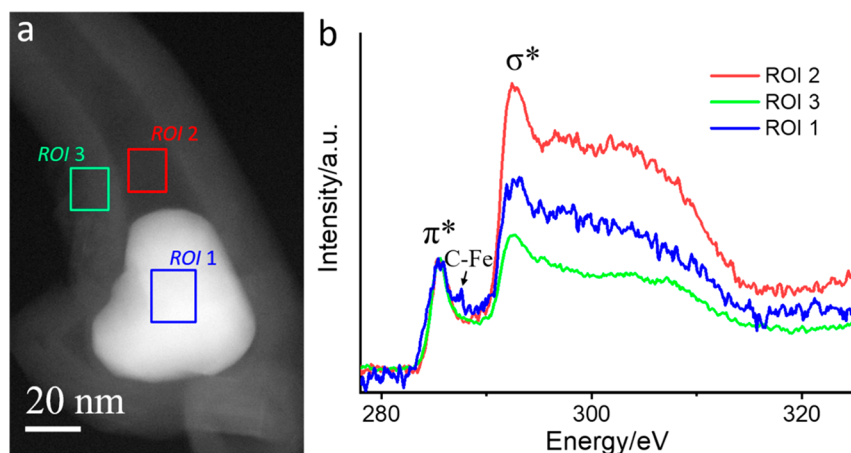


**Figure 3.** (a) HAADF-STEM image of a CNT with a catalytic particle encapsulated. (b) EELS spectra recorded from regions indicated in (a). All EELS spectra are normalized based on their  $\pi^*$  excitations.

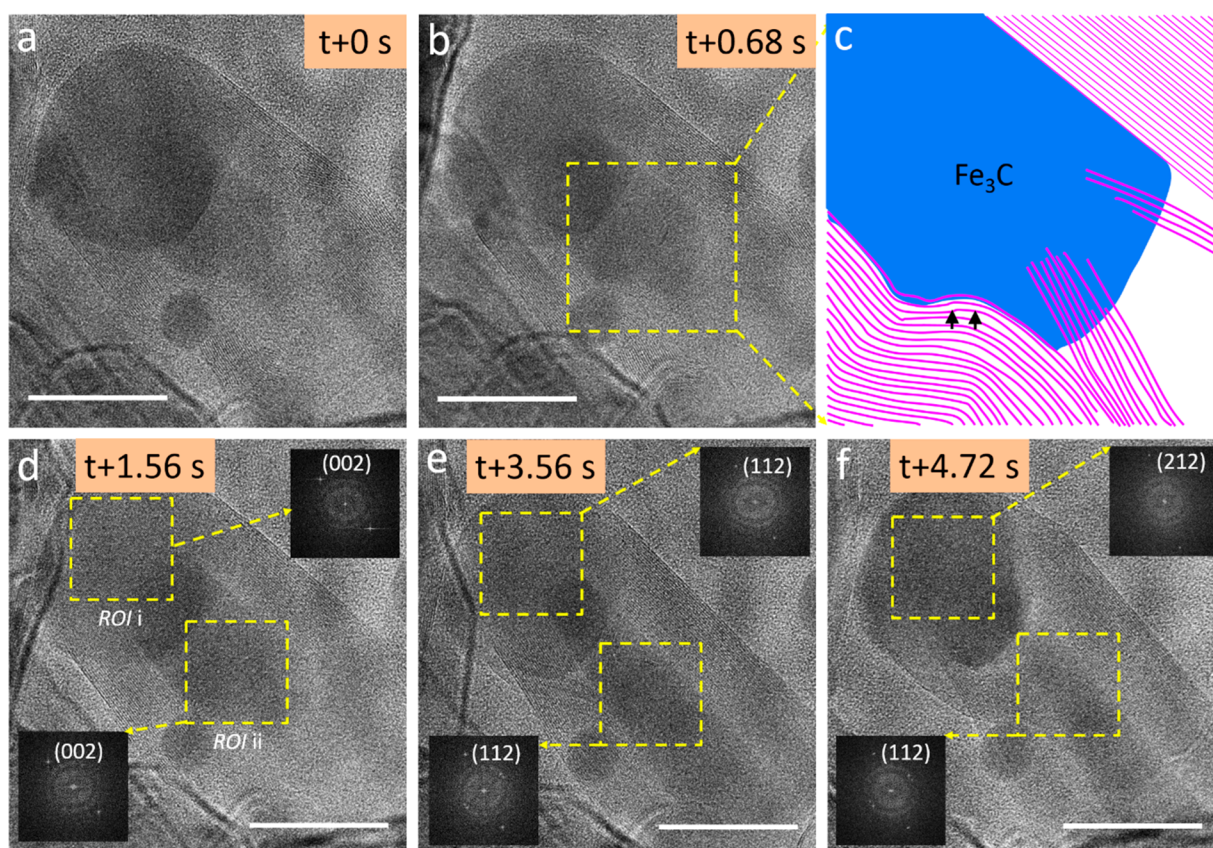


**Figure 4.** (a,b,d–f) In situ atomic-scale TEM observation of the catalyst splitting during the course of CNT growth; insets of (d–f) show FFTs from the indicated areas. (c) Schematic drawing of an elongated particle bonded with CNT layers. Scale bar is 20 nm.

growth speed. Because we are analyzing a two-dimensional (2D) projection of a 3D process, and the fact that different particles have different local environments, it is difficult to draw a definite conclusion about the effect of particle size on growth speed. However, based on our limited statistical analysis, we conclude that there is no strong effect of particle size on growth speed. In addition, in situ observation reveals that the catalyst splitting can take place in the process of CNT growth (Figure S4). With a small portion of the catalyst getting trapped into the growing CNT, the main part stays put and keeps catalyzing the CNT growth. Extended in situ observation further reveals that the catalyst splitting can occur multiple

times and eventually result in the growth termination of CNT. We will discuss this point later in more detail in the paper.

Identifying the structure of the catalyst under its functioning state is of central importance for understanding the growth mechanism of CNT. However, due to the complexity of the system the structure of the catalyst is still unclear or under debate. So far, both metallic iron and carbide have been proposed to be the active phases in CNT growth.<sup>22–24,32</sup> To provide insights about the structure of the catalyst, we carry out real-time observation of the working catalyst at atomic-scale (Movie 2). Figure 2a–d shows consecutive high-resolution TEM (HRTEM) images of a growing MWCNT

from a catalytic particle. The presence of lattice fringes further confirms the solid state of the catalyst. Analysis of the HRTEM images together with the fast Fourier transformation (FFT) patterns (Figures 2i–l) and image simulations (insets of Figure 2e–h) reveals that the catalyst exists as  $\text{Fe}_3\text{C}$  in an orthorhombic structure (cementite, space group:  $Pnma$ ). Another set of in situ data is shown Figure S5, which delivers a similar result. In this case, the shrinkage of the catalyst size is induced by the catalyst splitting.

Electron energy loss spectroscopy (EELS) is conducted in order to further demonstrate the formation of carbide phase. Figure 3a shows a high-angle annular dark-field scanning TEM (HAADF-STEM) image of a CNT nanotube grown from an iron catalyst during an in situ experiment. The carbon  $K$  edges from the catalytic particle (ROI 1) and two different regions (ROI 2, 3) of CNT are shown in Figure 3b. It needs to be mentioned that the EELS from ROI 1 actually contains a sum of contributions from both, catalytic particle and coated carbon layers. Comparison of all EELS spectra shows that in addition to the common presence of  $\pi^*$  (about 285.4 eV) and  $\sigma^*$  (about 292.4 eV) peaks, the EELS spectrum of ROI 1 also shows a unique peak located at about 287.6 eV. It is ascribed to the transition from 1s to C 2p–Fe 3d hybrid state,<sup>33</sup> thus confirming the formation of carbide. In addition, the carbon  $\pi^*$  peak from ROI 1 is slightly broader compared to these recorded from ROI 2 and 3 of CNT, which is probably due to the superposition of carbon signals from both carbide particle and graphitic carbon layers. The Fe  $L$  edge from catalytic particle is also recorded (Figure S6), which fits to that of carbide phase reported in a previous work.<sup>34</sup>

Therefore, based on above in situ observations and the associated structural and EELS analyses we are able to exclusively conclude that the cementite  $\text{Fe}_3\text{C}$  is the active structure in MWCNT growth at near ambient pressure. Additionally, analysis of time-resolved FFTs suggests that the crystal orientation of the catalyst changes dramatically during CNT growth. The zone axis of the catalyst changes from  $[-45-3]$  to  $[528]$  by  $106.72^\circ$  (Figure 2i,j) and further to  $[14-2]$  by  $82.87^\circ$  (Figure 2k). The rotation of the catalyst gives rise to strong swing of the growing CNT as well as the formation of twisted segments in CNT (see Movie 2).

We have mentioned above that catalytic splitting can occur during CNT growth. In the following, we show more details at atomic-scale the process of the catalyst splitting and discuss the possible reason for that. The HRTEM image (Figure 4a) extracted from Movie 3 reveals that the splitting starts with the formation of a tail structure at the apex of the catalyst. Instead of contracting back to the main catalyst to minimize the total energy of the system, continuous elongation toward the CNT growth direction occurs preferentially (Figure 4b,d,e). Closer observation indicates that the surface of the tail is anchoring with some carbon layers (Figure 4c). The presence of highly curved CNT walls according to the shape of tail (see black arrows) is also an indication for the anchoring. It is assumed that as long as the anchoring strength is strong enough to compensate the energy increase, the elongation will continue. Note that the elongation leads to a shrinkage in diameter of the tail, especially at the interfacial region between the tail and the main catalyst, and at a certain moment, the connection is broken (Figure 4f). It is also noted that prior to the fracture, a new CNT segment starts to grow, which rotates by a certain angle with reference to the former one. This twisted growth would favor the formation of neck zone between two adjacent

segments of CNT. It promotes separation of the tail from the parent catalyst due to Nichols–Mullins instability driven by high chemical potential of this zone.<sup>35</sup> It is also interesting to find that although the catalyst changes its crystallographic orientation in a random fashion, a coherence of crystallographic orientation between the tail and the main catalyst maintains as long as they are connected. The region i (head) and ii (tail) in Figure 4d show almost identical FFTs in which the diffraction spots can be assigned to  $\{002\}$  plane of  $\text{Fe}_3\text{C}$ . In Figure 4e, although the crystal orientation differs from the previous one, it remains the same for both the head and the tail of the catalyst. The diffraction spots in FFTs fit well to the  $\{112\}$  plane of  $\text{Fe}_3\text{C}$ . However, once the tail is separated from the main catalyst, the coherence disappears, as shown in Figure 4f.

On the basis of above observations, we can make a few statements about Fe-catalyzed CVD growth of MWCNTs at near ambient pressure. We reveal that the catalyst is in a highly fluctuating state in the process of CNT growth (Figure 1g). Although partially behaving like a liquid, the catalyst is in a solid state, which crystallizes as  $\text{Fe}_3\text{C}$  instead of metallic Fe (Figure 2). The  $\text{Fe}_3\text{C}$  phase is stable under the current experimental condition and no decomposition occurs. The MWCNT shows a similar growth speed of each cylinder layers, indicating a bulk diffusion of carbon species through the catalyst. Additionally, we show that catalyst splitting is a general phenomenon in the process of CNT growth (Figure S4). It leads to a decrease in the catalyst size and a shrinkage in diameter/wall number of the CNT (Figure S7).

In the following, we would like to briefly discuss the growth behavior of MWCNT based on above in situ observations. The MWCNT growth essentially follows a vapor–solid–solid (VSS) process,<sup>36</sup> given the observation that the catalyst is always in a solid state. Briefly speaking, hydrocarbon ( $\text{C}_2\text{H}_4$ ) absorbs and decomposes on the open surface of the solid catalyst to form active carbon species that subsequently diffuse into the catalyst (Figure S8a). When the catalyst reaches its supersaturated state, the dissolved carbon precipitates out and crystallizes in the form of graphene cylinders. Our kinetic study reveals that the growth velocity of CNT varies in an oscillatory manner, suggesting that the carbon diffusing rate through the carbon/catalyst interface changes periodically. This is likely caused by the fluctuation of carbon concentration in the active catalyst due to an unstable carbon supply from the gas phase to the catalyst. Sharma et al. observed a similar kinetic behavior in cobalt-catalyzed single-walled CNT (SWCNT) growth.<sup>37</sup> They revealed that both, metal and carbide, coexist in the catalytic particle, and their variation in volume ratio coincides with the fluctuated growth rate of SWCNT. However, in the present study of Fe-catalyzed MWCNT growth only  $\text{Fe}_3\text{C}$  is witnessed. The absence of metal phase may be related to its short lifetime, which makes it difficult to capture. Alternatively, it may be the case that the metallic Fe is not formed in the catalyst. Instead of fluctuating between metal and carbide as reported in the cobalt case, the iron catalyst may be changing between stoichiometric  $\text{Fe}_3\text{C}$  and carbon-deficient  $\text{Fe}_3\text{C}_{1-x}$  during CNT growth. It is also noted that the catalyst shows different levels of dynamic behavior from apex to base, which could be related to the different carbon concentration across the catalyst (Figure S8b). The apex of the catalyst is assumed to contain slightly less carbon content comparing to the base, considering that continuous growth of CNT from the apex would result in fluctuation of carbon concentration ( $\text{Fe}_3\text{C}$ – $\text{Fe}_3\text{C}_{1-x}$ ) in that

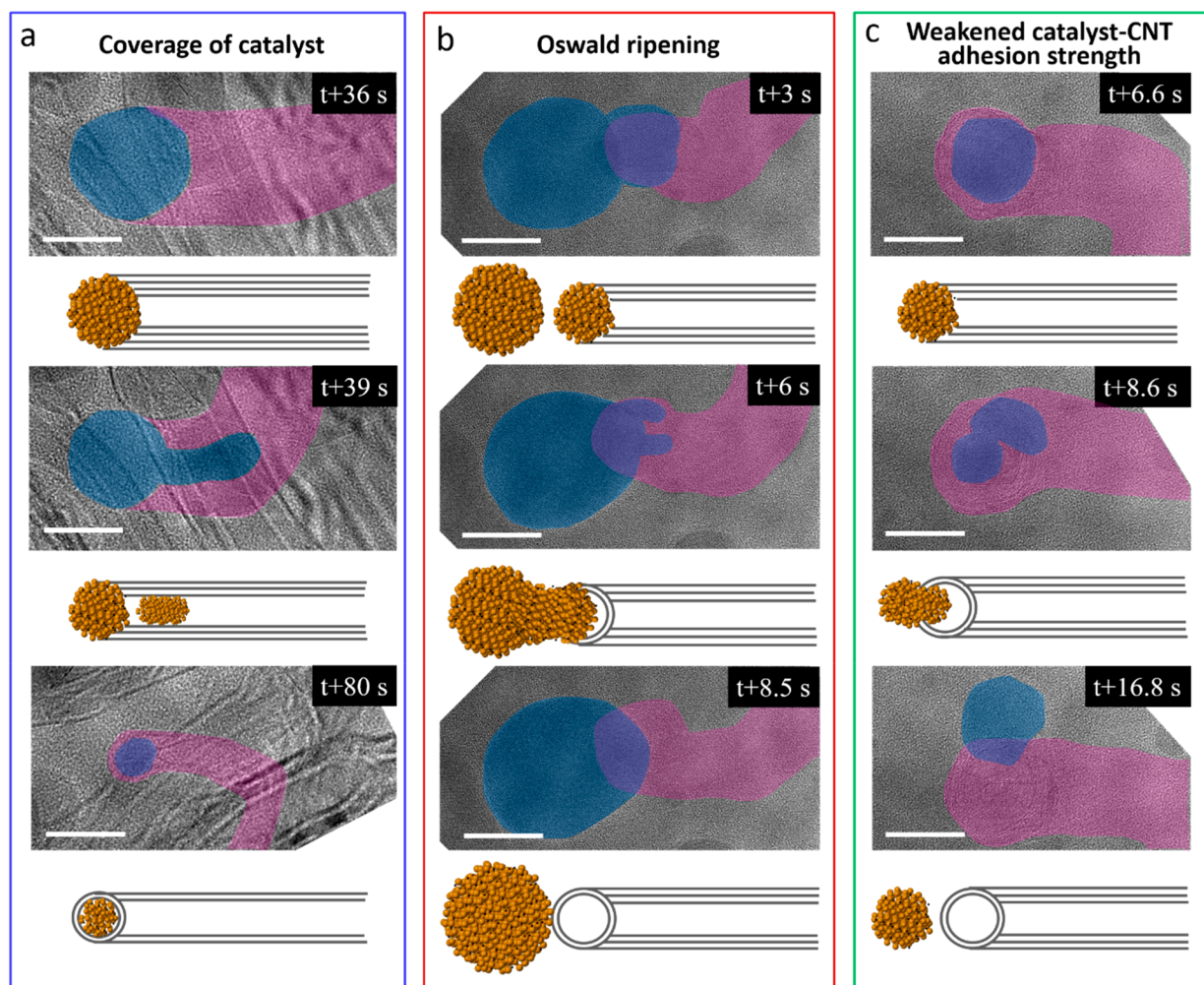


**Figure 5.** Growth termination of MWCNTs by (a) complete coverage of the catalyst, and dislocation of the catalyst from growing CNTs induced by (b) Oswald ripening and (c) weakened adhesion strength between the catalyst and CNT. Scar bar is 10 nm.

area. Moreover, presence of the static state at the base of the catalyst indicates a more stable component, that is, stoichiometric  $\text{Fe}_3\text{C}$ . We believe that the concentration gradient of carbon in the catalyst is responsible for the continuation of the CNT growth.

Growing long CNTs (mm to cm) has received an increasing level of attention because of its importance in both fundamental research and technical applications.<sup>38,39</sup> In order to grow long CNTs, it is essential to understand the deactivation mechanism of the catalyst in process of CNT growth. Previous studies have proposed that the complete coverage of the catalyst due to the presence of excessive carbon is responsible for the deactivation of the catalyst and the subsequent ceasing of CNT growth.<sup>40</sup> Because the hypothesis was made based on postcharacterizations, the transition process from active to inactive state of the catalyst is still missing. In addition, Kim et al. suggested<sup>41</sup> that the growth termination of SWCNT arrays may originate from Ostwald ripening and subsequent subsurface migration of catalytic particles from growth front of CNTs. However, whether it applies for the growth of MWCNTs is unknown. Thus, direct insights about the termination mechanism of MWCNTs are highly desirable.

In this regard, we perform extended in situ observations to monitor the whole CNT growth process until the ceasing of

CNT growth. On the basis of this study, we are able to demonstrate three different scenarios for the growth termination of CNTs (Figure 5). The first scenario (Figure 5a) is generally consistent with the previous postulation, that is, encapsulation of the catalyst by carbon layers, which blocks the carbon feeding path to the catalyst and leads to the growth termination. However, we additionally reveal that before the growth terminates, the catalytic particle undergoes several splitting events, resulting in a significant decrease in particle size from 15.5 to 5 nm (Movie 4). Shortly after the final splitting, the enclosure of the catalyst by additional carbon layers sets in, which terminates the CNT growth. This observation strongly indicates that catalytic splitting can promote the growth termination of CNT, which can be understood by the fact that a particle with smaller size is easier to be covered by excessive carbon species compared to a bigger one.

The other two scenarios are revealed due to out-migration of the catalyst from growing CNT. It occurs in two different manners, as shown in Figure 5b,c, respectively. In the scenario shown in Figure 5b, growth termination occurs through deformation and diffusion of the catalyst from growing CNT toward a neighboring particle that has a larger diameter, followed by a coarsening process (see Movie 5). This observation suggests that the out-diffusion of the catalyst is

driven by the Oswald ripening, which is in agreement with the previous discussion on the SWCNT case.<sup>41</sup> Alternatively, we demonstrate in Figure 5c that the catalyst may just diffuse out from the growing tube without joining any other particles afterward (Movie 6). In fact, there are no particles even surrounded, therefore assuredly ruling out the Oswald ripening. The reason for this phenomenon is still unclear to us. However, the observation of a rapid CNT growth after a short pause (before the initiation of the catalyst migration) indicates that the carbon transportation through the catalytic particle is highly unbalanced. This could weaken the catalyst–CNT adhesion strength<sup>26,40</sup> and lead to the detachment of CNT from the catalyst or vice versa.

**Conclusion.** In summary, in situ TEM has been utilized to study the Fe-catalyzed MWCNT growth and termination processes at near ambient pressure. We assuredly demonstrate that the catalyst at work is in solid state and crystallizes as cementite Fe<sub>3</sub>C. Moreover, we reveal that the catalyst presents distinct levels of dynamic behavior from the base to the apex during the course of CNT growth; with the apex of the catalyst showing a liquid-like deformation, the base of the catalyst remains faceted without showing any morphological change. Considering the presence of oscillatory growth kinetic of CNT, we further propose that the carbon concentration in the catalyst is fluctuating during CNT growth. Continuous monitoring of CNT growth uncovers three possible scenarios for the growth termination of CNT. First, we show that the full coverage of the catalyst by carbon layers can lead to deactivation of the catalyst and ceasing of CNT growth. We additionally reveal that prior to the encapsulation the catalyst goes through several splitting events, giving rise to a significant shrinkage of the catalyst size. This facilitates the carbon coverage of the catalyst and the growth termination of CNT. Second, we show that the termination can be induced by the Oswald ripening which drives the diffusion of the catalyst from growing CNT toward a neighboring particle of a bigger size. Third, we demonstrate that the catalyst particle can simply diffuse out from growing CNT without merging into other particles. We rationalize this phenomenon by the reduced adhesion strength between CNT and the catalyst as a result of an unbalanced carbon transportation in the catalyst. The presented in situ TEM results provide atomic-level insights into understanding of the growth and termination mechanisms of CNTs at more relevant conditions. It may serve as an important reference for controlled synthesis of CNTs via optimizations of both the catalyst design and experimental condition.

**Experimental Section.** *In Situ TEM Experiment.* The in situ TEM sample was prepared by drop-casting suspension of Fe<sub>2</sub>O<sub>3</sub> onto a MEMS-based heating chip which was then mounted into an in situ gas and heating holder (DENSolutions). The in situ experiments were performed inside the column of a FEI Titan 80-300 TEM (operated at 300 kV) using the in situ climate holder and a home-built gas feeding system. Before growing CNTs, we first treated the loaded Fe<sub>2</sub>O<sub>3</sub> in 10% H<sub>2</sub> at temperatures up to 800 °C and pressures up to 250 mbar in the nanoreactor. Afterward, we dropped down the temperature to 150 °C and switched the gas mixture from H<sub>2</sub>/He (10%/90%) to the reaction gas containing 20% H<sub>2</sub>, 20% C<sub>2</sub>H<sub>4</sub>, and 60% He. When the pressure inside of the nanoreactor was stabilized, the sample was stepwise heated up to 800 °C to initiate the CNT growth. In the present work, all movies of CNT growth were recorded using a Gatan OneView

camera. The growth behavior was studied at 800 °C, at a pressure of about 178.65 mbar and a flow rate of 0.24 mL/min. We have investigated the effect of the electron beam on the growth dynamics by changing magnification and illumination conditions. No obvious beam-induced artifacts could be observed in the dose range between  $1 \times 10^3$  and  $7 \times 10^5$  e/nm<sup>2</sup>s, which was used for the data presented in this work.

**EELS Measurement.** The EELS spectra were recorded from an aberration-corrected JEOL ARM-300F TEM (equipped with a Gatan GIF Quantum ER Dual EELS system) during an in situ experiment under a similar experimental condition as described above. Before acquisition, we first dropped down the temperature to 300 °C and then removed all gases from the nanoreactor.

**HRTEM Image Simulation.** The HRTEM image simulation was performed using JEMS software developed by Dr. P. Stadelmann. The cementite Fe<sub>3</sub>C structural file used for image simulation was downloaded from the Inorganic Crystal Structure Database (ICSD) with Collection Code 99002.<sup>42</sup>

**Growth Length and Velocity Measurements.** For growth length measurement of CNT based on Movie 1, we first identified a reference feature on CNT in the first frame and measured the length ( $L_1$ ) between this feature and the base of the catalyst. In the next frame, we located exactly the same feature and measured again the length ( $L_2$ ) from the feature to the base of the catalyst. The difference between two measured values ( $L = L_2 - L_1$ ) is thus the growth length of CNT between the time of two consecutive frames (0.04 s). Following this procedure, we did measurements sequentially for all adjacent frames. By summing them up and relating to the time used, we can therefore plot the length of CNT as a function of time, as shown in Figure 1h (red dotted line). It is worth mentioning that the reference feature selected on CNT is not necessary to be always the same for different pairs of adjacent frames. The important criterion for the selection is to make sure that the chosen reference feature can be clearly identified and located in two adjacent frames. After plotting the growth length as a function of time, the growth rate was obtained directly by performing the time-derivative of length using OriginPro 2018 (version b9.5.0.193), as shown in Figure 1h (blue dotted line).

## ■ ASSOCIATED CONTENT

### 📄 Supporting Information

The Supporting Information is available free of charge on the ACS Publications website at DOI: 10.1021/acs.nanolett.9b01888.

Structural characterization of Fe<sub>2</sub>O<sub>3</sub> powder; a series of TEM images showing collapse of big particles into smaller ones; sequential TEM images showing initiation of CNT growth; sequential TEM images showing the catalyst splitting; structural characterization of an active catalyst; EELS analysis; TEM images showing size-dependent wall number of CNT; schematic illustration of CNT growth (PDF)

Video of CNT growth and catalyst reshaping (AVI)

Video showing atomic structure of an active catalyst during CNT growth (AVI)

Video of the catalyst splitting during CNT growth (AVI)

Video showing CNT growth termination by catalyst encapsulation (AVI)

Video showing CNT growth termination via Oswald ripening (AVI)

Video showing CNT growth termination by weakened CNT–catalyst adhesion (AVI)

## AUTHOR INFORMATION

### Corresponding Author

\*E-mail: [xing.huang@scopem.ethz.ch](mailto:xing.huang@scopem.ethz.ch); [xinghuang0214@mail.ipc.ac.cn](mailto:xinghuang0214@mail.ipc.ac.cn).

### ORCID

Xing Huang: 0000-0002-8700-0606

Marc-Georg Willinger: 0000-0002-9996-7953

### Notes

The authors declare no competing financial interest.

## ACKNOWLEDGMENTS

We acknowledge the financial and instrumental support from Fritz Haber Institute of Max Planck Society and Scientific Center for Optical and Electron Microscopy of ETH Zurich.

## REFERENCES

- (1) De Volder, M. F. L.; Tawfick, S. H.; Baughman, R. H.; Hart, A. J. *Science* **2013**, *339* (6119), 535–539.
- (2) Jorio, A.; Dresselhaus, G.; Dresselhaus, M. S. *Carbon Nanotubes: Advanced Topics in the Synthesis, Structure, Properties and Applications*; Springer: Berlin, 2008.
- (3) Guo, T.; Nikolaev, P.; Thess, A.; Colbert, D. T.; Smalley, R. E. *Chem. Phys. Lett.* **1995**, *243* (1), 49–54.
- (4) Cassell, A. M.; Raymakers, J. A.; Kong, J.; Dai, H. *J. Phys. Chem. B* **1999**, *103* (31), 6484–6492.
- (5) Iijima, S. *Nature* **1991**, *354* (6348), 56–58.
- (6) Nessim, G. D. *Nanoscale* **2010**, *2* (8), 1306–1323.
- (7) Zhang, Q.; Huang, J.-Q.; Zhao, M.-Q.; Qian, W.-Z.; Wei, F. *ChemSusChem* **2011**, *4* (7), 864–889.
- (8) Helveg, S.; López-Cartes, C.; Sehested, J.; Hansen, P. L.; Clausen, B. S.; Rostrup-Nielsen, J. R.; Abild-Pedersen, F.; Nørskov, J. K. *Nature* **2004**, *427*, 426.
- (9) Yamada, T.; Namai, T.; Hata, K.; Futaba, D. N.; Mizuno, K.; Fan, J.; Yudasaka, M.; Yumura, M.; Iijima, S. *Nat. Nanotechnol.* **2006**, *1*, 131.
- (10) Zhang, Q.; Zhao, M.-Q.; Tang, D.-M.; Li, F.; Huang, J.-Q.; Liu, B.; Zhu, W.-C.; Zhang, Y.-H.; Wei, F. *Angew. Chem., Int. Ed.* **2010**, *49* (21), 3642–3645.
- (11) Huh, Y.; Lee, J. Y.; Cheon, J.; Hong, Y. K.; Koo, J. Y.; Lee, T. J.; Lee, C. J. *J. Mater. Chem.* **2003**, *13* (9), 2297–2300.
- (12) Flahaut, E.; Govindaraj, A.; Peigney, A.; Laurent, C.; Rousset, A.; Rao, C. N. R. *Chem. Phys. Lett.* **1999**, *300* (1), 236–242.
- (13) Chiang, W.-H.; Mohan Sankaran, R. *Nat. Mater.* **2009**, *8*, 882.
- (14) Zhang, S.; Kang, L.; Wang, X.; Tong, L.; Yang, L.; Wang, Z.; Qi, K.; Deng, S.; Li, Q.; Bai, X.; Ding, F.; Zhang, J. *Nature* **2017**, *543*, 234.
- (15) Wang, X.; Jiang, Q.; Xu, W.; Cai, W.; Inoue, Y.; Zhu, Y. *Carbon* **2013**, *53*, 145–152.
- (16) Tang, D.-M.; Kvashnin, D. G.; Cretu, O.; Nemoto, Y.; Uesugi, F.; Takeguchi, M.; Zhou, X.; Hsia, F.-C.; Liu, C.; Sorokin, P. B.; Kawamoto, N.; Mitome, M.; Cheng, H.-M.; Golberg, D.; Bando, Y. *Ultramicroscopy* **2018**, *194*, 108–116.
- (17) Jourdain, V.; Bichara, C. *Carbon* **2013**, *58*, 2–39.
- (18) Baylet, A.; Marécot, P.; Duprez, D.; Castellazzi, P.; Groppi, G.; Forzatti, P. *Phys. Chem. Chem. Phys.* **2011**, *13* (10), 4607–4613.
- (19) Lebedev, D.; Pineda-Galvan, Y.; Tokimaru, Y.; Fedorov, A.; Kaeffer, N.; Copéret, C.; Pushkar, Y. *J. Am. Chem. Soc.* **2018**, *140* (1), 451–458.
- (20) Kandemir, T.; Girgsdies, F.; Hansen, T. C.; Liss, K.-D.; Kasatkin, I.; Kunkes, E. L.; Wowsnick, G.; Jacobsen, N.; Schlögl, R.; Behrens, M. *Angew. Chem., Int. Ed.* **2013**, *52* (19), 5166–5170.
- (21) Huang, X.; Wang, Z.-J.; Weinberg, G.; Meng, X.-M.; Willinger, M.-G. *Adv. Funct. Mater.* **2015**, *25* (37), 5979–5987.
- (22) Hofmann, S.; Blume, R.; Wirth, C. T.; Cantoro, M.; Sharma, R.; Ducati, C.; Hävecker, M.; Zafeirotos, S.; Schnoerch, P.; Oestereich, A.; Teschner, D.; Albrecht, M.; Knop-Gericke, A.; Schlögl, R.; Robertson, J. *J. Phys. Chem. C* **2009**, *113* (5), 1648–1656.
- (23) Wirth, C. T.; Bayer, B. C.; Gamalski, A. D.; Esconjauregui, S.; Weatherup, R. S.; Ducati, C.; Baetz, C.; Robertson, J.; Hofmann, S. *Chem. Mater.* **2012**, *24* (24), 4633–4640.
- (24) Yoshida, H.; Takeda, S.; Uchiyama, T.; Kohno, H.; Homma, Y. *Nano Lett.* **2008**, *8* (7), 2082–2086.
- (25) Sharma, R.; Moore, E.; Rez, P.; Treacy, M. M. J. *Nano Lett.* **2009**, *9* (2), 689–694.
- (26) Zhang, L.; He, M.; Hansen, T. W.; Kling, J.; Jiang, H.; Kauppinen, E. I.; Loiseau, A.; Wagner, J. B. *ACS Nano* **2017**, *11* (5), 4483–4493.
- (27) Lin, M.; Tan, J. P. Y.; Boothroyd, C.; Loh, K. P.; Tok, E. S.; Foo, Y.-L. *Nano Lett.* **2007**, *7* (8), 2234–2238.
- (28) Jiang, Y.; Li, H.; Wu, Z.; Ye, W.; Zhang, H.; Wang, Y.; Sun, C.; Zhang, Z. *Angew. Chem., Int. Ed.* **2016**, *55* (40), 12427–12430.
- (29) Vendelbo, S. B.; Elkjær, C. F.; Falsig, H.; Puspitasari, I.; Dona, P.; Mele, L.; Morana, B.; Nelissen, B. J.; van Rijn, R.; Creemer, J. F.; Kooyman, P. J.; Helveg, S. *Nat. Mater.* **2014**, *13*, 884.
- (30) Niu, Y.; Liu, X.; Wang, Y.; Zhou, S.; Lv, Z.; Zhang, L.; Shi, W.; Li, Y.; Zhang, W.; Su, D. S.; Zhang, B. *Angew. Chem., Int. Ed.* **2019**, *58* (13), 4232–4237.
- (31) Kumar, M.; Ando, Y. *J. Nanosci. Nanotechnol.* **2010**, *10* (6), 3739–3758.
- (32) He, Z.; Maurice, J.-L.; Gohier, A.; Lee, C. S.; Pribat, D.; Cojocaru, C. S. *Chem. Mater.* **2011**, *23* (24), 5379–5387.
- (33) Furlan, A.; Jansson, U.; Lu, J.; Hultman, L.; Magnuson, M. J. *Phys.: Condens. Matter* **2015**, *27* (4), 045002.
- (34) Jin, Y.; Xu, H.; Datye, A. K. *Microsc. Microanal.* **2006**, *12* (2), 124–134.
- (35) Pigos, E.; Penev, E. S.; Ribas, M. A.; Sharma, R.; Jakobson, B. I.; Harutyunyan, A. R. *ACS Nano* **2011**, *5* (12), 10096–10101.
- (36) Persson, A. I.; Larsson, M. W.; Stenström, S.; Ohlsson, B. J.; Samuelson, L.; Wallenberg, L. R. *Nat. Mater.* **2004**, *3* (10), 677–681.
- (37) Lin, P. A.; Gomez-Ballesteros, J. L.; Burgos, J. C.; Balbuena, P. B.; Natarajan, B.; Sharma, R. *J. Catal.* **2017**, *349*, 149–155.
- (38) Zhang, R.; Wen, Q.; Qian, W.; Su, D. S.; Zhang, Q.; Wei, F. *Adv. Mater.* **2011**, *23* (30), 3387–3391.
- (39) Zhang, R.; Zhang, Y.; Zhang, Q.; Xie, H.; Qian, W.; Wei, F. *ACS Nano* **2013**, *7* (7), 6156–6161.
- (40) Aguiar-Hualde, J.-M.; Magnin, Y.; Amara, H.; Bichara, C. *Carbon* **2017**, *120*, 226–232.
- (41) Kim, S. M.; Pint, C. L.; Amama, P. B.; Zakharov, D. N.; Hauge, R. H.; Maruyama, B.; Stach, E. A. *J. Phys. Chem. Lett.* **2010**, *1* (6), 918–922.
- (42) Wood, I. G.; Vocadlo, L.; Knight, K. S.; Dobson, D. P.; Marshall, W. G.; Price, G. D.; Brodholt, J. *J. Appl. Crystallogr.* **2004**, *37* (1), 82–90.